ACS APPLIED MATERIALS & INTERFACES

RESEARCH ARTICLE

www.acsami.org

Crystal Structure, Phase, and Electrical Conductivity of Nanocrystalline $W_{0.95}Ti_{0.05}O_3$ Thin Films

N. R. Kalidindi,[†] F. S. Manciu,[‡] and C.V. Ramana*[,†]

[†]Department of Mechanical Engineering, Energy Systems Laboratory (ESL), and [‡]Department of Physics, University of Texas at El Paso, El Paso, Texas 79968, United States

ABSTRACT: $W_{0.95}Ti_{0.05}O_3$ films were fabricated using sputter-deposition onto Si(100) wafers in by varying the growth temperature from room temperature (RT) to 500 °C. X-ray diffraction (XRD), high-resolution scanning electron microscopy (SEM) coupled with energy-dispersive X-ray spectrometry (EDS), and Raman spectroscopy (RS) were performed to investigate the effect of temperature on the growth behavior, crystal structure, texturing, surface morphology, and chemical bonding of $W_{0.95}Ti_{0.5}O_3$ films. The results indicate that the effect of temperature is significant on the growth and microstructure of $W_{0.95}Ti_{0.05}O_3$ films. XRD results indicate that the effect of Ti is remarkable on the crystallization of WO_3. $W_{0.95}Ti_{0.05}O_3$ films grown at temperatures <300 °C are amorphous compared to pure WO_3 crystalline films crystallizing at 200 °C. Phase transformation is induced in $W_{0.95}Ti_{0.05}O_3$ resulting in tetragonal structure at ≥300 °C. The structural changes were also reflected in the intensities of −W−O−W− vibrational modes in RS measurements. The SEM imaging analysis indicates that the phase transformations are accompanied by a characteristic change in surface morphology. Room temperature electrical conductivity of $W_{0.95}Ti_{0.05}O_3$ films increases from 0.63 to 27 $(\Omega\ m)^{-1}$ with increasing temperature from RT to 400 °C due to improved structural order. Electrical conductivity exhibit a decrease at 500 °C (7.4 $(\Omega\ m)^{-1}$) due to disordering induced by Ti segregation, which is confirmed by XRD and RS measurements.

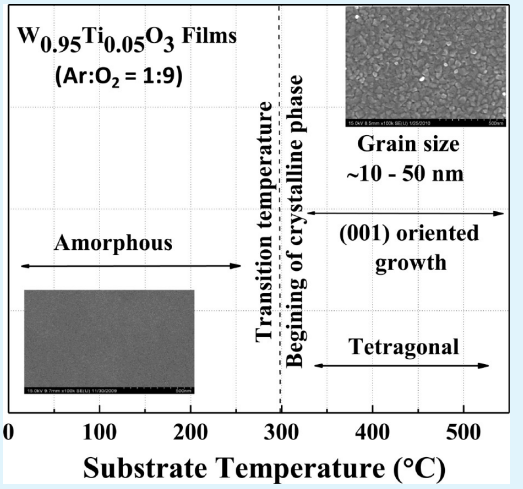

KEYWORDS: WO_3, Ti-doping, microstructure, phase transformations, H_2S sensors

1. INTRODUCTION

Semiconducting oxides have received significant recent attention as sensor materials because of their remarkable electrical properties sensitive to oxidative or reductive type of gases.[1−5] Currently, there has been a great deal of interest in WO_3 low-dimensional structures for a wide variety of applications in chemical and mechanical sensors, selective catalysis, electrochemical industry and environmental engineering.[1−7] It has been demonstrated that the sensing properties of WO_3 films will have numerous applications in environmental and industrial pollution monitoring. WO_3 films exhibit excellent functional activity to various gases, such as H_2S, NO_x, trimethylamine, and other organics, and are suitable for integrated sensors.[6−9] Most importantly, WO_3 nanocrystalline films have been established as one of the best gas sensors for the reducing gases such as NO_2, H_2, and CO and the results evidenced the role of the microstructure specifically the grain size.[6−9]

The search for novel materials for chemical sensors with enhanced performance has led the scientific community that works in the field to consider ternary compounds of metal-oxide semiconductors as potential candidates.[10] A leading criterion would be starting with a metal-oxide semiconductor that has already proven sensing capability, such as WO_3 in this case, and adding another properly chosen metal. Searching for new materials should be accompanied by a thorough study of the microstructural and electronic properties of the materials under consideration. In the context of the effort described herein, the present work was performed on the Ti-doping effects in a small and controlled amount into WO_3 to produce $W_{0.95}Ti_{0.05}O_3$. The focus of the investigation was to explore the effects of Ti and temperature on the growth behavior, microstructure, and electrical characteristics. The details of growth behavior, microstructure and electronic properties of pure WO_3 films and preliminary results on the Ti-doping effects were reported elsewhere.[11−14]

W−Ti alloy films have already been proven to exhibit low electrical resistance, thermal stability, oxidation resistance, inertness, good adhesion towards metal contact and the substrate, and high refractive index.[15−17] Therefore, investigating the fundamental aspects of microstructure evolution and structure−property relationships in W−Ti−O films may provide opportunities to tailor the microstructure and properties of the materials for the desired application, as well as optimization for chemical sensors. Interestingly, we found that Ti inhibits the crystallization, increases the temperature for crystal growth, and inhibits the

Received: December 8, 2010
Accepted: January 24, 2011
Published: February 16, 2011

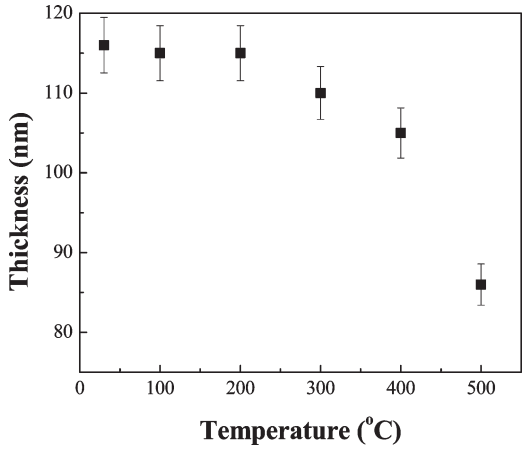

Figure 1. $W_{0.95}Ti_{0.05}O_3$ film thickness variation with substrate temperature. It is evident from the curve that the films grown at RT−200 °C exhibit more or less constant thickness. A decrease in film thickness at $T_s \geq 300$ °C is due to crystallization and improved density.

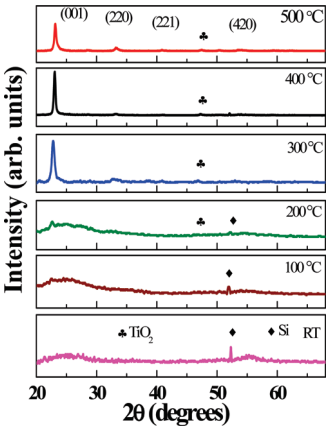

Figure 2. XRD patterns of $W_{0.95}Ti_{0.05}O_3$ films. It is evident from the curves that the films grown at RT-300 °C are amorphous whereas films grown at $T_s \geq 300$ °C are nanocrystalline. $W_{0.95}Ti_{0.05}O_3$ films crystallize in tetragonal phase as indicated by the XRD patterns for $T_s \geq 300$ °C.

grain growth compared to pure WO_3 films. The results obtained are presented and discussed in relation to microstructure and electrical properties in $W_{0.95}Ti_{0.05}O_3$ films.

2. EXPERIMENTAL SECTION

A. Fabrication. $W_{0.95}Ti_{0.05}O_3$ thin films were deposited onto silicon (Si) (100) wafers by radio-frequency (RF) (13.56 MHz) magnetron sputtering. The Si(100) substrates were cleaned by RCA (Radio Corporation of America) cleaning. All the substrates were thoroughly cleaned and dried with nitrogen before introducing them into the vacuum chamber, which was initially evacuated to a base pressure of $\sim 1 \times 10^{-6}$ Torr. Tungsten−titanium ($W_{0.95}Ti_{0.05}$) alloy target (Plasmaterials Inc.) of 2 in. diameter and 99.95% purity was employed for reactive sputtering. $W_{0.95}Ti_{0.5}$-target was placed on a 2-inch sputter gun, which is placed at a distance of 8 cm from the substrate. A sputtering power of 40 W was initially applied to the target while introducing high purity argon (Ar) into the chamber to ignite the plasma. Once the plasma was ignited the power was increased to 100 W and oxygen (O_2) was released into the chamber for reactive deposition. The flow of the Ar and O_2 and their ratio was controlled using MKS mass flow controllers. Before each deposition, $W_{0.95}Ti_{0.05}$ target was pre-sputtered for 10 min using Ar alone with shutter above the gun closed. The deposition was made for 1 h. The samples were grown at different temperatures (T_s) varying from room temperature (RT) to 500 °C. The substrates were heated by halogen lamps and the desired temperature was controlled by Athena X25 controller.

B. Characterization. The grown $W_{0.95}Ti_{0.5}O_3$ films were characterized by performing structural and electrical measurements. X-ray diffraction (XRD) measurements on $W_{0.95}Ti_{0.5}O_3$ films were by performed using a Bruker D8 Advance X-ray diffractometer. All the measurements were made ex situ as a function of growth temperature. XRD patterns were recorded using Cu Kα radiation (λ = 1.54056 Å) at RT. The coherently diffracting domain size (d_{hkl}) was calculated from the integral width of the diffraction lines using the well known Scherrer's equation after background subtraction and correction for instrumental broadening. The Scherrer equation is[18]

$$d_{hkl} = 0.9\lambda/\beta\cos\theta \quad (1)$$

where d_{hkl} is the size, λ is the wavelength, β is the width of a peak at half of its intensity, and θ is the angle of the peak.

Surface imaging analysis was performed using a high-performance and ultra high resolution scanning electron microscope (Hitachi S-4800). The secondary electron imaging was performed on $W_{0.95}Ti_{0.05}O_3$ films grown on Si wafers using carbon paste at the ends to avoid charging problems. The grain detection, size-analysis and statistical analysis was performed using the software provided with the SEM.

The Raman measurements were acquired at ambient conditions with an *alpha 300 WITec* confocal Raman system, using the 532 nm excitation of a Nd:YAG laser. An acquisition time of 5s for each spectrum and a 100× objective lens with a NA = 0.95 was used in all experiments.

DC electrical resistivity measurements were carried out under the vacuum of 1×10^{-2} Torr by two-probe method in a home-made setup. Resistance was measured by employing a Keithley electrometer. The point contacts were made by soldering the indium metal at the corners of the films.

3. RESULTS AND DISCUSSION

A. Film Thickness. $W_{0.95}Ti_{0.05}O_3$ thin films were found to be uniform and well-adherent to the substrate surface. All the samples exhibit a mixed yellowish-blue color. $W_{0.95}Ti_{0.05}O_3$ film thickness variation with T_s is shown in Figure 1. It is evident that the film thickness is not very sensitive to T_s until 300 °C, at which point thickness decreases slightly as T_s increases to 500 °C. We attribute this observed characteristic feature to the structural modifications in the grown films as function of T_s. $W_{0.95}Ti_{0.05}O_3$ film thickness is almost constant at T_s = RT−200 °C. However, a marked decrease in film thickness can be noted at $T_s \geq 300$ °C. From XRD and SEM measurements discussed in the later sections, the $W_{0.95}Ti_{0.05}O_3$ thin films in the constant thickness up to 200 °C were amorphous while those grown at $T_s \geq 300$ °C were crystalline. This suggests that the observed change in film thickness is due to crystallization and densification with increasing substrate temperature.

B. Crystal Structure. X-ray diffraction patterns of $W_{0.95}Ti_{0.05}O_3$ thin films are shown in Figure 2 as a function of T_s. The XRD curve (Fig. 2) of $W_{0.95}Ti_{0.05}O_3$ films grown at T_s = RT−200 °C did not show any peaks indicating their characteristic amorphous (a-$W_{0.95}Ti_{0.05}O_3$) nature. The diffraction peak begins to appear in XRD pattern when T_s = 300 °C indicating the film crystallization at this temperature. The intense peak corresponds to the tetragonal phase of WO_3 indicating that the $W_{0.95}Ti_{0.05}O_3$ films crystallize in tetragonal structure. The crystallization temperature noted for Ti-doped WO_3 films is higher when compared to that of pure WO_3 films grown using sputter-deposition.[11−13] We reported

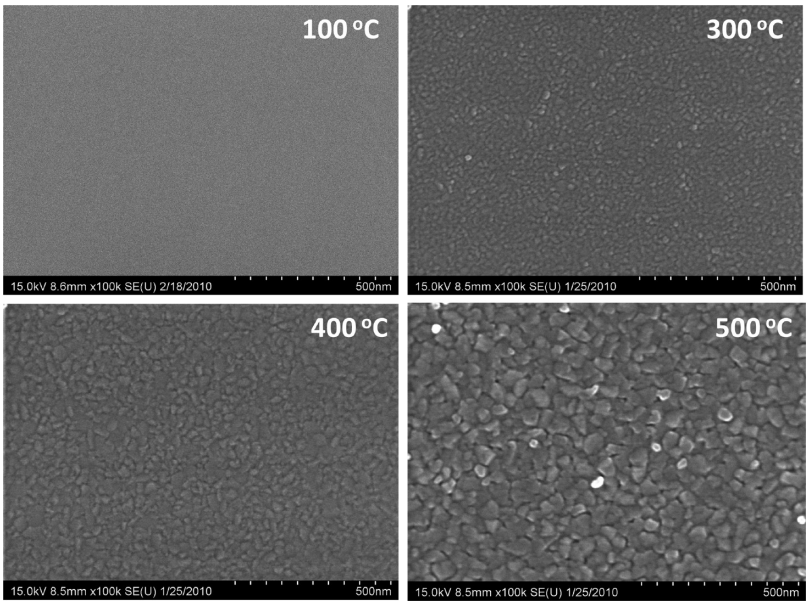

Figure 3. The high-resolution SEM images of $W_{0.95}Ti_{0.05}O_3$ films as a function of substrate temperature. It is evident from the images that the surface morphology of $W_{0.95}Ti_{0.05}O_3$ films is sensitive to the growth temperature. The morphological changes are correlated with the changes in crystal structure and specific phase formation of $W_{0.95}Ti_{0.05}O_3$ films as a function of growth temperature.

previously that pure WO_3 films crystallize at T_s = 100−200 °C.[11−13] The effect of Ti is remarkable in preventing crystallization of WO_3 and raises its crystallization temperature. The XRD peak is rather broad indicating the presence of nanocrystallites. It is evident (Figure 2) that the intensity of the peak which corresponds to diffraction from (001) planes increases with increasing T_s. This is indicative of an increase in the average crystallite-size and preferred orientation of the film along (00l) with increasing T_s. This behavior is quite similar to that observed in pure WO_3 films.[11] The preferred *c*-axis orientation of $W_{0.95}Ti_{0.05}O_3$ films could be due to the growth process minimizing the internal strain-energy in the film.[12,19,20] Anisotropy exists in crystalline materials and the strain energy densities will typically be different for different crystallographic directions. The growth will favor those orientations with low strain energy density.[12,19−21] Therefore, increasing T_s favors the preferred orientation along (00l) while minimizing the strain-energy in the $W_{0.95}Ti_{0.05}O_3$ films. The most important feature that can be noted is the formation of a small amount of TiO_2 phase for the films grown at T_s = 400−500 °C. Note that the peak becomes broad at T_s = 500 °C.

The preferred growth of $W_{0.95}Ti_{0.05}O_3$ films, as seen in XRD, allows calculating the relative strain factor using the XRD data. The strain factor (Γ), which is derived from the lattice mismatch, is calculated using the formula

$$\Gamma = \frac{d_{(100)\mathrm{Si}} - d_{(001)\mathrm{sample}}}{d_{(001)\mathrm{sample}}}\% \qquad (2)$$

The strain factor Γ is found to be ∼3% for the samples grown at T_s = 300−500 °C. The observed strain can be understood in terms of the combined effect of two factors. Effective increase in the number of atoms due to surface and interface effects for the reduced dimensions of the nanocrystallites is the first. The stabilization of the crystal formation and lattice parameters with increasing T_s is the later.

C. Surface, Interface Morphology, and Growth Behavior. The high-resolution SEM images of $W_{0.95}Ti_{0.05}O_3$ films as a function of T_s are shown in Figure 3. The amorphous nature resulting from disordering induced by Ti is clearly evident in the SEM images of $W_{0.95}Ti_{0.05}O_3$ films grown at T_s = RT−200 °C. A fine microstructure and uniform distribution of dense spherical particles can be seen in $W_{0.95}Ti_{0.05}O_3$ films grown at T_s = 300−500 °C. The observed average grain size variation with T_s is shown in Figure 4a. It must be emphasized that the grain size indicated at 200 °C is based on the fact that the SEM images have occasionally shown the grains of ≤6 nm which are embedded in the amorphous matrix. However, most of the film volume is amorphous and didn't reveal even a sign of localized structural order with other spectroscopic or X-ray diffraction analysis. Most significant point is the remarkable effect of temperature on the surface morphology of $W_{0.95}Ti_{0.05}O_3$ films. Based on thickness variation, SEM and XRD data as a function of T_s, the growth behavior of $W_{0.95}Ti_{0.05}O_3$ films can be conveniently divided into two zones, where the morphology differences are significant. The first category or zone contains the set of $W_{0.95}Ti_{0.05}O_3$ films grown at temperatures <300 °C. The second is the set of $W_{0.95}Ti_{0.05}O_3$ films grown at temperatures ≥300 °C. No features can be seen for $W_{0.95}Ti_{0.05}O_3$ films grown at RT even at very high magnifications (Figure 3a). This observation is in agreement with the XRD results indicating the complete amorphous nature of the samples. If temperature is low such that the period of the atomic jump process of adatoms on the substrate surface is very large, the condensed species may stay stuck to the regions where they are landing thus leading to an amorphous $W_{0.95}Ti_{0.05}O_3$ films. The adatom mobility on the surface increases with increasing temperature. The small, dense particles spherical in shape can be noticed in SEM images for $W_{0.95}Ti_{0.05}O_3$ films grown at 300−400 °C. The SEM data along with appearance of diffraction peaks in XRD clearly indicate that 300 °C is the critical temperature to promote the growth of nanocrystalline $W_{0.95}Ti_{0.05}O_3$ films. For the given set of experimental conditions, a temperature of 300 °C is, therefore, favorable to provide sufficient energy for $W_{0.95}Ti_{0.05}O_3$ crystallization.

The XRD and SEM results suggest that a further increase in temperature beyond 300 °C results in changes in the crystal

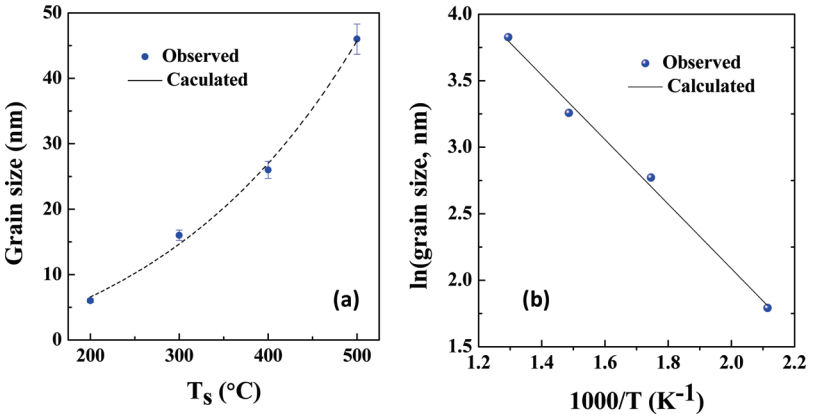

Figure 4. (a) Variation in grain size of $W_{0.95}Ti_{0.05}O_3$ films with substrate temperature. The circles represent the experimental data while the line represents the fit to the exponential function according to eq 3. (b) Ln(grain size) vs $1 \times 10^3/T$ plot for the data shown in panel a. Solid line represents the linear fit. Excellent agreement between the observed data and linear fit suggests the thermally activated growth process of sputter-deposited $W_{0.95}Ti_{0.05}O_3$ films.

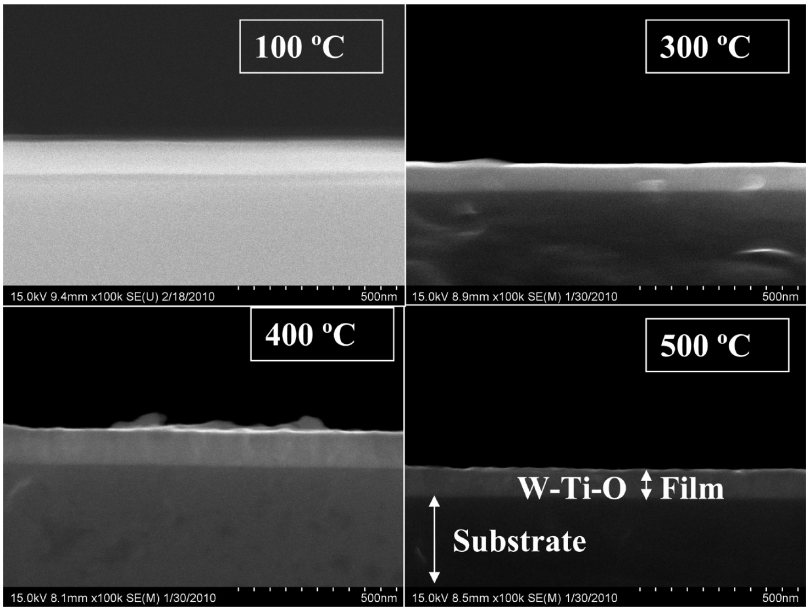

Figure 5. Si−$W_{0.95}Ti_{0.05}O_3$ interface cross-sectional SEM images of $W_{0.95}Ti_{0.05}O_3$ films grown at various temperatures. The Si substrate and $W_{0.95}Ti_{0.05}O_3$ film regions are as indicated.

structure and morphology. $W_{0.95}Ti_{0.05}O_3$ films continue to show preferred growth along with an increase in average particle size with increasing T_s. A functional relationship obtained between the average particle size (L) and the temperature fits to an exponential growth function (Figure 4b). The data supports thermally activated growth process of nanocrystalline $W_{0.95}Ti_{0.05}O_3$ films. Therefore, similar to the diffusion coefficient equation[22,13] L can be expressed as

$$L = L_o \exp(-\Delta E/k_B T) \quad (3)$$

where L is the average particle size, L_0 is a pre-exponential factor or proportionality constant which depends on the specific film, substrate materials involved, ΔE the activation energy, k_B the Boltzmann constant, and T the absolute temperature. The data analysis and Arrehenius plot are presented in Figure 4b, where the data points and a linear fit to the data are shown. It is important to recognize the functional linear relationship which is an indicative of thermally driven growth of nanocrystalline $W_{0.95}Ti_{0.05}O_3$ films. The activation energy derived from the slope of the linear fit (Figure 4b) is ~0.21 eV, which is higher than that reported for pure WO_3 films.[13]

The cross-sectional SEM images of $W_{0.95}Ti_{0.5}O_3$−Si interfaces for $W_{0.95}Ti_{0.5}O_3$ films grown at various temperatures are shown in Figure 5. The $W_{0.95}Ti_{0.5}O_3$ film and Si-substrate regions are as indicated in Figure 5 for a representative sample. The cross-sectional SEM images indicate that the $W_{0.95}Ti_{0.5}O_3$ films grow in a columnar structure on Si surfaces.

D. Local Structure, Chemical Bonding, and Composition. The EDS spectra of representative $W_{0.95}Ti_{0.05}O_3$ films as a function of T_s are shown in Figure 6. The spectra indicate the characteristic X-ray peaks (as labeled in Figure 6) corresponding to W, Ti, and O atoms present in the sample. The absence of any other peaks except those due to W and O indicate that the sample consists exclusively of W−Ti oxide phase. It is well-known that

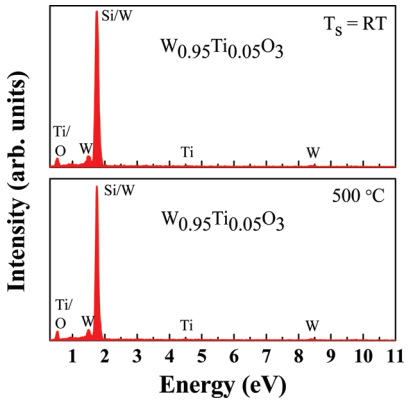

Figure 6. EDS spectra of $W_{0.95}Ti_{0.05}O_3$ films. The peaks due to X-rays emitted from W, Ti, and O present in the films are as labeled.

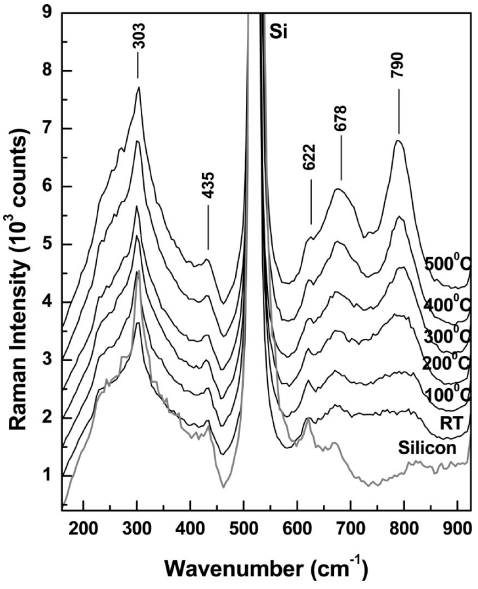

Figure 7. Raman spectra of $W_{0.95}T_{0.i5}O_3$ films grown at various temperatures.

the X-rays generated are characteristic of the atoms.[23,24] Therefore, the detection of x-rays emitted from the sample as a result of sample-electron beam interaction provides the identification of the atoms present in the crystal. The emitted x-ray peaks detected are only from W and O while the peak due to Si substrate is serving as a reference. No other elements were detected, which is a sign of high purity $W_{0.95}Ti_{0.05}O_3$ films without any elemental impurities incorporated from chemical processing or post-preparation handling.

The results of Raman measurements of $W_{0.95}Ti_{0.05}O_3$ samples grown at Si substrate temperatures between RT (bottom spectrum) and 500 °C (top spectrum) are presented in Figure 7. Besides clear spectroscopic evidence of the most intense Si vibration at 522 cm^{-1}, the spectra of $W_{0.95}Ti_{0.05}O_3$ samples also show the existence of Si−O bonds at 303, 435, 622, and 675 cm^{-1}. For easier comparison and association of these latter features with the influence of Si, in Figure 6, we also present the Raman spectrum of the substrate alone (gray line).

Although the spectra of $W_{0.95}Ti_{0.05}O_3$ samples recorded for growth temperatures less than 200 °C largely resemble the Si

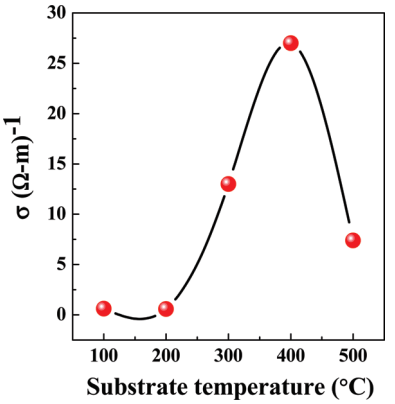

Figure 8. Variation in electrical conductivity of $W_{0.95}Ti_{0.05}O_3$ films with substrate temperature.

spectrum, which demonstrates the amorphous nature of these samples, the slight increase and sharpening at higher temperatures of the intensities of the two broad bands centered around 678 and 790 cm^{-1} reveal a trend towards ordering and crystallization of the material. These features transform into definite Raman peaks at 400 and 500 °C. Not only do Raman data corroborate with our previous observations of continuing crystallization with increasing temperature, but from the position of the 790 cm^{-1} Raman vibration we can infer in our samples a morphological transformation of pure WO_3 with Ti doping. This affirmation is based on an approximately 20 cm^{-1} shift between the 790 cm^{-1} feature and the typical W−O stretching mode of pure WO_3, previously observed in our work around 810 cm^{-1}.[25] Similar behavior, namely a frequency decrease in the position of this Raman peak, was reported in the literature for Ti-doped WO_3.[26] Unfortunately, because of the relatively strong influence of the Si substrate, no detectable Ti−O bonds were observed in our $W_{0.95}Ti_{0.05}O_3$ Raman spectra to confirm the formation of TiO_2 as observed in the XRD measurements.

E. Electrical Characteristics. The room temperature electrical characteristics of $W_{0.95}Ti_{0.05}O_3$ films are shown in Fig. 8. It can be seen that with increasing T_s up to 400 °C the conductivity increases, which is due to improvement in the crystal structure of $W_{0.95}Ti_{0.05}O_3$ films. A small decrease in conductivity value at T_s = 500 °C could be due to the formation of excess TiO_2, as evidenced in XRD data. The electrical resistivity is reported to increase with size-reduction due to the increasing grain boundary volume and associated impedance to the flow of charge carriers.[27−31] If the crystallite size is smaller than the electron mean free path, grain boundary scattering dominates and hence the resistivity increases. The resistivity is also very sensitive to lattice imperfections in solids, such as vacancies and dislocations that are present in nanocrystalline materials.[11] In addition to that, lattice strain and the distortions can affect the motion of charge causing a increase in resistivity.[27−31] The substrate temperature dependence of the conductivity data observed for $W_{0.95}Ti_{0.05}O_3$ can be explained taking these factors into consideration. $W_{0.95}Ti_{0.05}O_3$ films grown at T_s = RT-200 °C are amorphous. The randomness or disordered structure of the films induced by Ti, therefore, accounts for the observed conductivity of a-$W_{0.95}Ti_{0.05}O_3$ films. An increase in conductivity with increasing growth temperature can be attributed to the structural transformation from amorphous to tetragonal phase and the preferred orientation of the film along (001). In addition, a decrease in strain energy of the growing $W_{0.95}Ti_{0.05}O_3$ film, as discussed using the XRD results, with increasing temperature also causes the increase in

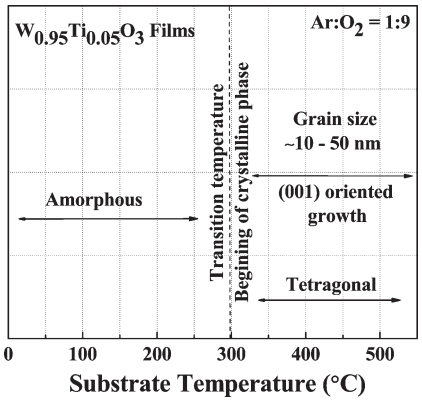

Figure 9. Phase diagram summarizing the microstructure evolution of $W_{0.95}Ti_{0.05}O_3$ films as a function of temperature.

conductivity. Finally, based on the XRD, SEM, EDS, and RS measurements, we propose the phase diagram for the microstructure evolution of $W_{0.95}Ti_{0.05}O_3$ thin films as shown in Figure 9. The phase diagram summarizes the observed structural changes as a function of substrate temperature and could provide a roadmap while considering the $W_{95}Ti_5O_3$ thin films for the desired set of electronic or sensor applications.

4. SUMMARY AND CONCLUSIONS

$W_{95}Ti_5O_3$ thin films were fabricated using sputter-deposition and their structural and electrical properties were investigated in detail. The effect of temperature is significant on the growth behavior, surface morphology, crystal structure and electrical characteristics of $W_{95}Ti_5O_3$ thin films. With increasing temperature, the $W_{95}Ti_5O_3$ films are seen to transform from amorphous to tetragonal structure. The amorphous-to-crystalline transition temperature is 300 °C for $W_{0.95}Ti_{0.5}O_3$ films which is higher than that for pure WO_3 films (200 °C). The structural studies demonstrate that the effect of Ti is remarkable on the crystallization of WO_3. Phase transformation is induced in $W_{0.95}Ti_{0.05}O_3$ resulting in tetragonal structure at ≥300 °C. The morphological changes associated with the structural transformations were confirmed by the Raman spectroscopic measurements. Room temperature electrical conductivity of $W_{0\cdot95}Ti_{0.05}O_3$ films increases from 0.63 to 27 $(\Omega\ cm)^{-1}$ with increasing temperature from RT to 400 °C because of improved structural order. The observed decrease in electrical conductivity at 500 °C (7.4 $(\Omega\ cm)^{-1}$) is due to disordering induced by Ti segregation, which is confirmed by XRD. On the basis of the results obtained in this work, a phase diagram for the microstructure evolution in $W_{0.95}Ti_{0.05}O_3$ thin films is proposed.

AUTHOR INFORMATION

Corresponding Author

*E-mail: rvchintalapalle@utep.edu.

ACKNOWLEDGMENT

This material is based on work supported by the Department of Energy under Award DE-PS26-08NT00198-00. Hitachi 4800 SEM used for the morphology and X-ray chemical analysis of Ti-doped WO_3 samples in this work was acquired through the support from National Science Foundation (NSF-DMR-0521650). The support from National Science Foundation to acquire *alpha 300 WITec* confocal Raman system through Grant 0723115 is gratefully acknowledged.

REFERENCES

(1) Zhu, L.F.; She, J.C.; Luo, J.Y.; Deng, S.H.; Chen., J.; Xu, N.S. *J. Phys. Chem. C* **2010**, *114*, 15504–15509.
(2) Wang, L.; Teleki, S. E.; Pratsinis, S. E.; Gouma, P. I. *Chem. Mater.* **2008**, *20*, 4794–4796.
(3) Wolcott, A.; Kuykendall, T.R.; Chen, W.; Chen, S.; Zhang, J.Z. *J. Phys. Chem. B* **2006**, *110*, 25288–25296.
(4) Li, X.; Lou, T.-J.; Sun, X.-M.; Li, Y.-D. *Inorg. Chem.* **2004**, *43*, 5442–5449.
(5) Wang, X.; Miura, N.; Yamazoe, N. *Sens. Actuators, B* **2000**, *66*, 74–79.
(6) Tatsuma, T.; Saitoh, S.; Ohko, Y.; Fujishima, A. *Chem. Mater.* **2001**, *13*, 2838–2842.
(7) Szilgyi, I.M.; Madarsz, J.; Pokol, G.; Kirly, P.; Trknyi, G.; Saukko, S.; Mizsei, J.; Tth, A.L.; Szab., A.; Varga-Josepovits, K. *Chem. Mater.* **2008**, *20*, 4116–4125.
(8) Meixner, H.; Lampe, U. *Sens. Actuators, B* **1996**, *33*, 198–202.
(9) Baeck, S. H.; Jaramillo, T.; Stucky, G. D.; McFarland, E. W. *Nano Lett.* **2002**, *2*, 831–834.
(10) Ferroni, M.; Guidi, V.; Martinelli, G.; Nelli, P.; Sberveglieri, G. *Sens. Actuators, B* **1997**, *44*, 499–504.
(11) Vemuri, R. S.; Kamala Bharathi, K.; Gullapalli, S. K.; Ramana, C. V. *ACS Appl. Mater. Interfaces* **2010**, *2*, 2623–2628.
(12) Kalidindi, N.R.; Kamala Bharathi, K.; Ramana, C.V. *Appl. Phys. Lett.* **2010**, *97*, 142107.
(13) Gullapalli, S. K.; Vemuri, R. S.; Manciu, F. S.; Enriquez, J. L.; Ramana, C. V. *J. Vac. Sci. Technol., A* **2010**, *28*, 824–828.
(14) Gullapalli, S. K.; Vemuri, R. S.; Ramana, C. V. *Appl. Phys. Lett.* **2010**, *96*, 171903.
(15) Glebovsky, V. G.; Yu, V.; Yaschak; Baranov, V. V.; Sackovich, E. L. *Thin Solid Films* **1995**, *257*, 1–5.
(16) Guidi, V.; Boscarino, D.; Comini, E.; Faglia, G.; Ferroni, M.; Malagu, C.; Martnelli, G.; Rigato, V.; Sberveglieri, G. *Sens. Actuators, B* **2000**, *65*, 264.
(17) Bundaleski, N.; Petrovic, S.; Perusko, D.; Kovac, J.; Zalar, A. *Appl. Surf. Sci.* **2008**, *254*, 6390–6394.
(18) Cullity, B. D.; Stock, S. R., *Elements of X-Ray Diffraction*, 3rd ed.; Prentice-Hall: New York, 2001.
(19) Ramana, C. V.; Smith, R. J.; Julien, C. M. *J. Vac. Sci. Technol., A* **2004**, *22*, 2453–2458.
(20) Ramana, C. V.; Julien, C. M. *Chem. Phys. Lett.* **2006**, *428*, 114–118.
(21) Ramana, C.V.; Smith, R. J.; Hussain, O. M. *Phys. Status Solidi A* **2003**, *199*, R4–7.
(22) Kittel, C., *Introduction to Solid State Physics*; Wiley: New York, 1968.
(23) Ramana, C. V.; Ait-Salah, A.; Utsunomiya, S.; Mauger, A.; Gendron, F.; Julien, C.M *Chem. Mater.* **2007**, *19*, 5319–5324.
(24) Ramana, C. V.; Ait-Salah, C. V.; Utsunomiya, A.; Morhange, S.; Mauger, J. F.; Gendron, A.; Julien, F. *J. Phys. Chem. C* **2007**, *111*, 1049–1054.
(25) Manciu, F.S.; Enriquez, J.L.; Durrer, W.G.; Yun, Y.; Ramana, C. V.; Gullapalli, S.K, *J. Mater. Res.* **2010**, in press.
(26) Hu, Y.; Wang, L.; Li, G *Plasma Sci. Technol.* **2007**, *9*, 432.
(27) Depero, L.E.; Natali Sora, I.; Perego, C.; Sangaletti, L.; Sberveglieri, G. *Sens. Actuators, B* **1996**, *31*, 19–24.
(28) Wu, L.; Tien-Shou, W.; Chung-Chuang, W. *J. Phys. D: Appl. Phys.* **1980**, *13*, 259–266.
(29) Bakonyi, I.; Toth-Kadar, E.; Tarnoczi, T.; Varga, L.; Cziraki, A.; Gerocs, I.; Fogarassy, B. *Nanostruct. Mater.* **1993**, *3*, 155–158.
(30) Ambily, S.; Menon, C. S. *Thin Solid Film* **1999**, *347*, 284–289.
(31) Ajai Gupta, K.; Kumar, V.; Khare, N. *Solid State Sci.* **2007**, *9*, 817–823.